

Internal Energy Distribution of the NCO Fragment from Near-Threshold Photolysis of Isocyanic Acid, HNCO

Steven S. Brown, H. Laine Berghout, and F. Fleming Crim*

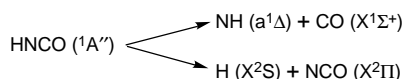
Department of Chemistry, University of Wisconsin—Madison, Madison, Wisconsin 53706

Received: September 12, 1995[⊗]

We report the first measurement of the vibrational- and rotational-state distributions in the NCO fragment resulting from photolysis of HNCO. Recent studies have drawn conclusions about the photochemistry of HNCO and the vibrational distribution in the NCO fragment from observations of the kinetic energy distribution of the H atom produced in this photolysis; however, there has been no direct observation of the NCO fragment itself. We use laser-induced fluorescence to detect the nascent NCO photoproducts and spectral simulations to extract vibrational-state populations. The rotational distributions, where we can measure them, show little excitation, and the vibrational energy preferentially appears in the bending mode. The vibrational-state distribution results directly from the excited-state geometry of the HNCO parent, in which the NCO group is bent. The dissociation proceeds from this bent NCO group to a linear NCO fragment, strongly exciting the bending mode. We find about 65% of the total energy in relative translation of the fragments, while 30% goes into vibration and 5% into rotation of NCO.

I. Introduction

The chemistry of isocyanic acid, HNCO, is both practically and fundamentally interesting. For example, HNCO removes deleterious NO_x compounds from exhaust gases after combustion, a process called RAPRENO_x (RAPid REDuction of NO_x).¹ The NCO radical, produced by abstraction of an H atom from HNCO by OH radicals present in the exhaust gas, seems to play a major role in the reduction of NO_x.² This chemistry has implications for dealing with issues such as photochemical smog and acid rain. The photochemistry of isocyanic acid is also fundamentally interesting because it has several excited-state decomposition pathways that involve different product electronic states and cleave different bonds. In particular, irradiation of HNCO at wavelengths below 242 nm produces either H + NCO or NH + CO photoproducts,^{3–6} where the NH radical is produced in its lowest singlet state rather in the ground triplet state,



The N–H dissociation threshold is $37\,630 \pm 420 \text{ cm}^{-1}$,⁷ and that for C–N singlet dissociation lies slightly higher at $41\,530 \pm 150 \text{ cm}^{-1}$.⁸

Recently, we reported the bond-selective photodissociation of isocyanic acid.^{9,10} In these experiments, we used a two-step excitation to the dissociative electronic surface (vibrationally mediated photodissociation)^{11,12} in which we first prepared a vibrationally excited N–H stretching state containing 3 or 4 quanta of excitation. Photodissociation of this state changed the branching ratio between the two channels, $\Phi_{\text{NCO}}/\Phi_{\text{NH}}$, by a factor of at least 17 in favor of the NCO channel relative to photodissociation of the ground vibrational state. In this experiment, we used laser-induced fluorescence (LIF) detection of both NH ($a^1\Delta$)^{13–15} and NCO ($X^2\Pi$)^{16–18} fragments and compared the relative intensities of each.

The NH ($a^1\Delta$) + CO ($X^1\Sigma^+$) channel in the photodissociation of HNCO has received considerable attention. Several authors

have measured the rotational, vibrational, and translational energy disposals of both the NH and CO fragments at a variety of photolysis wavelengths ranging from 230 to 193.3 nm,^{8,19–24} and all experiments are consistent with an impulsive dissociation on a steeply repulsive potential energy surface in which the NCO skeleton is bent rather than having its ground-state linear geometry. The other major photochemical channel in HNCO has received less experimental attention, despite the accessibility of the NCO fragment via LIF. A number of studies have focused on the measurement of the branching ratio between the two channels. Using kinetic measurements, Spiglanin *et al.* determined an upper limit to the quantum yield for NCO at 193.3 nm of $\Phi_{\text{NCO}} \leq 0.1$,⁸ and Yi and Bersohn later confirmed this value in measurements of H atom LIF subsequent to HNCO photodissociation at 193.3 and 212.6 nm. They found quantum yields of $\Phi_{\text{NCO}} = 0.05 \pm 0.006$ and $\Phi_{\text{NCO}} = 0.13 \pm 0.01$, respectively.²⁵ Earlier studies that measured the concentrations of final products from the reactions of the radicals produced in the initial photolysis step also found that the production of NH ($a^1\Delta$) dominates at short photolysis wavelengths but that the importance of the NCO channel increases at longer wavelengths.⁵ Our own study of this photochemistry, which measured the relative LIF signals of NCO and NH ($a^1\Delta$) fragments, found that the NCO channel dominates near the energetic threshold for production of NH ($a^1\Delta$) (240.8 nm) but that the quantum yield for NCO drops dramatically between 235 and 225 nm.¹⁰ A very recent study of the translational energy of the H atom produced in the photolysis of HNCO with 193.3-nm light determined that 70% of the available energy went into relative translation, 26% went into vibration of the NCO fragment, with a long progression in the bending mode, and 4% went into NCO rotation. These observations, like those for the NH + CO channel, are consistent with a rapid dissociation from an excited state with a bent NCO geometry.²⁶

The ultraviolet absorption in HNCO at photon energies that dissociate the molecule comes from a transition from the ground to the first excited singlet state, ${}^1A'' \leftarrow {}^1A'$ in C_s symmetry.^{27–29} The ground (${}^1A'$) state is planar and has a nearly linear N–C–O angle of 172° and an H–N–C angle of 124° .³⁰ The excited (${}^1A''$) state results from the promotion of an electron from the

[⊗] Abstract published in *Advance ACS Abstracts*, April 1, 1996.

2a'' orbital, which is primarily a combination of N and O atom p orbitals, to the antibonding 10 a' orbital. Because the energy of the 2a'' orbital is smallest for a linear NCO group and the minimum energy of the 10 a' orbital occurs for a bent NCO group,²⁹ the geometry of HNCO changes significantly upon excitation. Analysis of rotational structure at the low-energy end of the UV absorption spectrum suggests a bent NCO group in the excited state with a N–C–O angle of 119° for a *trans* configuration.²⁷

We directly observe the quantum-state distribution of the NCO fragment from the photolysis of HNCO at several different photolysis energies near the threshold for production of this fragment. There are a few recent studies of the gas-phase quantum-state distribution of the NCO fragment from other sources, including the reaction of fluorine atoms with isocyanic acid (F + HNCO),^{16,31} cyanide radicals with molecular oxygen (CN + O₂),^{18,32} and a flame of CH₄ and N₂O.¹⁷ The spectrum of NCO (X²Π) provides one of the few examples of the Renner–Teller effect, which couples the vibrational angular momentum from the degenerate bend in this linear triatomic molecule to the orbital angular momentum of the Π electronic state.^{33–37} Indeed, previous studies have found extensive excitation of the bend in NCO^{17,18} and have characterized both the Renner interaction and the Fermi resonance that occur between the states (v_1, v_2, v_3) and ($v_1 + 1, v_2 - 2, v_3$), where v_1 is the symmetric stretch, v_2 is the doubly degenerate bend, and v_3 is the antisymmetric stretch.^{38–40}

We are interested in determining the rotational and vibrational quantum-state populations in the NCO fragment from the photolysis of HNCO. A measurement of the nascent populations of the NCO photofragments helps reveal the dynamics that occur on the excited-state surface of HNCO. In our vibrationally mediated photodissociation experiments,^{10,41} we wish to measure the effect of exciting particular vibrational states in the parent HNCO on the dynamics of the photodissociation into the NCO channel, and we must first establish the quantum-state distributions that result from photodissociation out of the ground vibrational state.

II. Experimental Approach

The experimental apparatus is similar to one described previously for vibrationally mediated photodissociation of isocyanic acid,⁹ except that here we use only two lasers: one for photolysis of HNCO and one for detection of the NCO fragment by laser-induced fluorescence. The photolysis laser is a Nd:YAG laser pumped dye laser operating on a range of coumarin dyes with a frequency-doubled output in the range 240–260 nm and a pulse energy of ≤ 1 mJ. The probe laser is an XeCl excimer laser pumped dye laser that uses a series of stilbene and coumarin dyes to detect various vibrational states of NCO (X²Π) by laser-induced fluorescence. The energy of the probe laser is on the order of 100 μ J in a 10-ns pulse focused to a spot approximately 1 mm in diameter.

The largest source of uncertainty is the power drift in both the photolysis and probe lasers due to the short lifetime of the coumarin dyes. The problem was particularly pronounced for the photolysis laser, which had a higher overall pulse energy. We compensated for the resulting signal drift by monitoring the pulse energy of both lasers using photodiodes and normalizing the signal. We checked for consistency by scanning the NCO spectrum several times, scanning the spectral regions in a different order each time. The fluctuations in the normalized signal level were approximately 15–20% using this procedure, and we used this as the uncertainty in our measured vibrational-state populations of NCO.

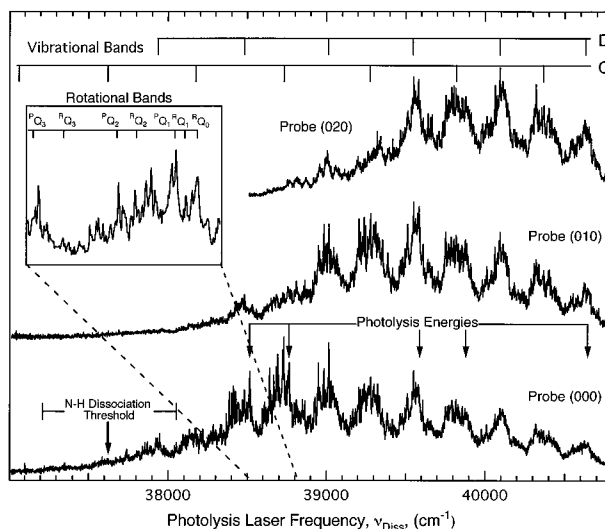


Figure 1. Photolysis yield spectrum of NCO (X²Π) fragments from HNCO photolysis in three different vibrational states: (000), (010), and (020). Vibrational and rotational assignments of the bands from Dixon (ref 27) appear over the spectra and the inset, respectively. The arrows on the lower trace mark the literature value for the N–H dissociation threshold (ref 7) and the photolysis energies used in this experiment.

We measured the effects of saturation by recording the intensities of NCO rotational lines in the spectrum of the ground vibrational state in a rotationally thermalized sample, which we obtained by introducing several microseconds of delay between the photolysis and probe lasers and increasing the sample pressure to 200 mTorr. Taking into account the effect of saturation on the anticipated line intensities using a simple three-state kinetic model,⁴² we adjusted the value of the spectral power density, ρ , in our simulations to fit the experimentally observed intensity distribution, assuming that it was a Boltzmann distribution with a temperature of 300 K. We then used this value of ρ to simulate the nascent distributions of rotational states using the expression for partially saturated rotational line strengths.^{32,42}

The photolysis and probe beams counterpropagated through a cylindrical fluorescence cell in which the pressure of isocyanic acid was 100 mTorr. The HNCO vapor flowed through this cell from a reservoir of liquid HNCO at -78 °C (dry ice/acetone bath) with a vapor pressure slightly under 1 Torr.⁴³ We verified that the photoproducts from the preceding laser shot did not interfere with our signal by placing the probe laser pulse slightly prior to the photolysis laser pulse and observing that there was no NCO LIF signal. For experiments measuring the nascent distribution of NCO fragments, the photolysis–probe delay was 30 ns, conditions under which we estimate that fewer than 3% of the NCO photofragments have a hard-sphere collision before detection. An *f*/1 optical system, photomultiplier tube, gated integrator, digital-to-analog converter, and laboratory computer collected and stored the fluorescence signals from NCO A(²Σ⁺) We synthesized HNCO by the dropwise addition of a saturated solution of potassium cyanate (KOCN) to concentrated phosphoric acid (H₃PO₄).⁴⁴ After condensing HNCO vapor in a trap at -196 °C, we distilled it twice between traps at -30 and -196 °C to remove water.

III. Results

A. Yield Spectra. Figure 1 shows the photofragment yield spectrum of NCO (X²Π) produced from HNCO photolysis. Each trace of this figure has the probe laser fixed on a transition originating in a different vibrational state in NCO (X²Π) and the photolysis laser scanned through the region of the dissociation threshold. Superimposed above the spectra are a series of

combs that mark the vibrational progressions that Dixon and Kirby²⁷ identified in the UV absorption spectrum of HNCO. They do not assign these progressions to any particular vibrations in the electronically excited state of HNCO but rather label them as A, B, C, and D. Because the A and B progressions occur primarily at lower energies in the UV absorption spectrum, below the threshold for dissociation of the N–H bond, we do not observe them in our yield spectrum. Progressions C and D, which begin near the N–H dissociation threshold, are clearly apparent in our spectra. The spacing between the bands in each of these progressions is approximately 500 cm^{-1} , suggesting that they are progressions in bending vibrations on the excited surface, consistent with the excited state having a minimum for a bent NCO geometry. The Franck–Condon factors should favor excitation of bending modes on such a surface. Dixon and Kirby suggested that the interleaving of two vibrational progressions might reflect the presence of *cis* and *trans* isomers in the excited state. The structure in each of the spectra probing different vibrational states in the NCO fragment is identical, except for the increase in the appearance thresholds for different vibrational states with increasing excitation in the NCO bending mode. The arrow on the left-hand side of the lower trace marks the measured threshold for NCO production⁷ and its uncertainty.

Dixon and Kirby's analysis of the UV spectrum included rotational as well as vibrational assignments. The rotational structure is quite diffuse, and they identified it primarily from the more well-defined structure at the low energy end of the UV spectrum below the NCO appearance threshold. The inset in Figure 1 is an expanded view of one of the vibrational bands in our photolysis yield spectrum of NCO (000), with the rotational assignments for this band²⁷ superimposed over the top. The rotational structure is not extremely clear because the bands are diffuse at this energy and there is a large amount of rotational congestion. Isocyanic acid in its ground state is a near-prolate top, with an asymmetry parameter $\kappa = 0.9996$.³⁰ The ground-state A rotational constant, 30.637 cm^{-1} , is quite large, and the K_a structure dominates the rotational bands in the spectrum since the energy spacing of different K_a states is intermediate between the bending vibrations and that of the J and K_c states.⁴⁵ Based on the observed rotational structure, Dixon²⁷ assigned the UV bands of HNCO to a perpendicular transition with prolate-top selection rules of $\Delta K = \pm 1$. The comb in the inset of Figure 1 marks the position of the Q branch transitions for different values of K. The notation of the markers is $^{\Delta K}\Delta J_K$. Because the A rotational constant is so large, only a small number of K states are populated in our room-temperature sample. The measured change in the magnitude of the A rotational constant from Dixon and Kirby's work is $\Delta A = -26\text{ cm}^{-1}$, which is consistent with the equilibrium geometry of the NCO group changing from nearly linear in the ground state to bent in the excited state.

B. NCO Spectroscopy. Renner–Teller interactions^{33,34} strongly influence the vibrational energy level structure of NCO ($X^2\Pi$). Hougen describes this interaction,³⁵ and here we give only a brief summary of the remarkably complex vibrational energy level structure of NCO. For a particular value of the bending quantum number, v_2 , the quantum number for the projection of the vibrational angular momentum along the molecular axis is l , which takes on the values $l = v_2, v_2 - 2, v_2 - 4, \dots, -v_2$. The Renner–Teller interaction couples the vibrational angular momentum to the orbital angular momentum, generating a new angular momentum quantum number, $K = \Lambda + l$. For example, with $v_2 = 2, l = 2, 0,$ and -2 , and $\Lambda = \pm 1$ in the Π electronic state, there are six different combinations

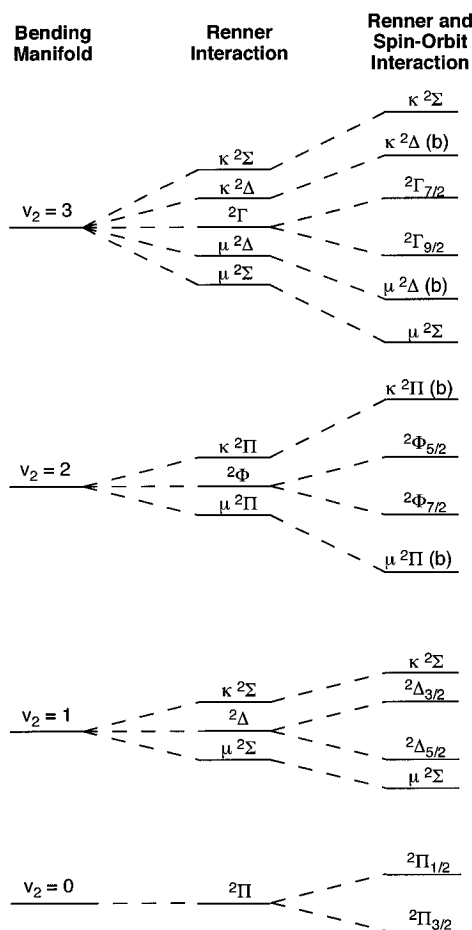


Figure 2. Vibronic energy level diagram of NCO ($X^2\Pi$) showing the Renner–Teller and spin–orbit interactions.

of l and Λ that give the values $K = 3, 1, 1, -1, -1,$ and -3 . These six states divide into three sets of two. There are two Π states, which are labeled μ and κ such that the κ states lie above the μ states in energy. There is also one unique Φ state corresponding to $K = v_2 + 1$. The spin–orbit interaction further splits these states into $P = K + \Sigma$ components, where $\Sigma = 1/2$ for the doublet spin state. The energy level diagram in Figure 2 illustrates these interactions and the energy ordering of the states for NCO, which has a negative spin–orbit parameter.³⁶

C. Product-State Distributions. We measured the product-state distribution of the NCO photofragments at five different photolysis energies near the threshold for cleavage of the N–H bond. The arrows on the lower trace in Figure 1 mark the different photolysis wavelengths, for which the available energy ranges from 890 to 3030 cm^{-1} , and which excite both C and D vibrational bands in the excited state of HNCO. In each case, we fix the photolysis laser wavelength on the blue edge of the vibrational band in order to excite the $K'' = 0, RQ_0$ band. This assures consistency in the rotational states excited for different bands since the sharp edge on the blue side of each vibrational band is the most prominent and easily identified feature, as the inset in Figure 1 shows.

The laser-induced fluorescence spectrum from nascent NCO fragments at the lowest photolysis energy ($h\nu_{\text{Diss}} = 38\,516\text{ cm}^{-1}$ or $E_{\text{avail}} = 890\text{ cm}^{-1}$ above threshold) is the lower trace of Figure 3, and a simulation of the bands is the upper trace. We used the simulation to determine the populations of different vibrational states in the experimental spectrum using the prescription described by Sauder *et al.*³² Table 1 lists the vibrational-state populations. There is little enough congestion in this spectrum

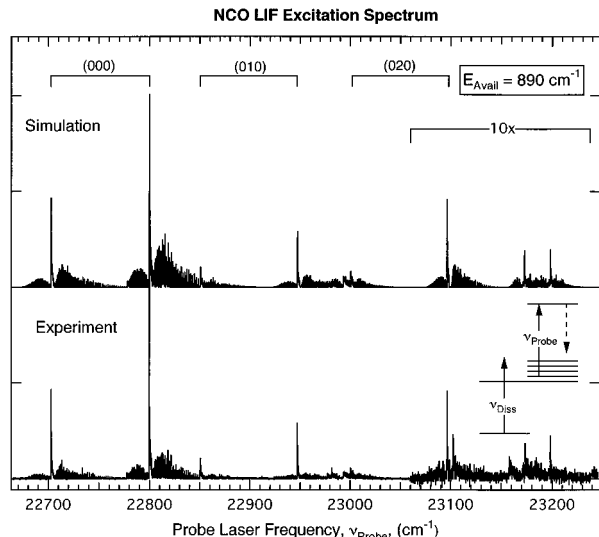


Figure 3. Laser-induced fluorescence spectrum of NCO ($X^2\Pi$) from HNCO photolysis at $E_{\text{avail}} = 890 \text{ cm}^{-1}$. The upper trace is a simulation of the spectrum that was used to extract vibrational populations from the experimental data. The combs over the top mark the positions of the P_2 and Q_1 bandheads belonging to the unique $K = v_2 + 1$ vibronic states that occur in the center of each v_2 manifold.

that it is relatively easy to pick out the individual rotational structure, particularly in the intense (000) bands, which are clearly the most populated at this low photolysis energy. The combs over the top of the spectrum mark the intense bandheads, which occur for the P_2 and Q_1 branches that belong to the unique $K = v_2 + 1$ states that occur for each value of v_2 .¹⁸ There is also a great deal of rotational structure, including numerous bandheads, arising from states with $K \neq v_2 + 1$ that is more apparent in spectra taken at higher photolysis energies, where there is greater population in states with $v_2 > 0$. However, we use the $K = v_2 + 1$ bandheads as convenient markers for each v_2 state since they are very intense and occur in the center of the manifold.

Using the rotational branches in the (000) manifold that are not badly overlapped, we fit the line intensities to a Boltzmann distribution to determine a rotational temperature. Such a distribution is not necessarily appropriate for the unrelaxed photolysis products, but the observed intensities fit this distribution remarkably well. We also considered an unbiased prior rotational distribution, taking into account only the rotational and translational densities of states for a given excess photolysis energy.^{46,47}

$$P^0(J) \propto (2J + 1) (E_{\text{rot}}(J) - E_{\text{vib}} - E_{\text{avail}})^{1/2}$$

In this expression, E_{rot} is the rotational energy as a function of J , E_{vib} is the vibrational energy, and E_{avail} is the total available excess energy from the photolysis. Figure 4 is a plot of the rotational populations obtained from the P_{12} , $Q_2 + R_{12}$, and R_2 branches in the (000) $^2\Pi_{1/2}(F_2)$ state as a function of J for two different photolysis energies. The solid lines are fits to a Boltzmann distribution with rotational temperatures of 225 K for the lower energy photolysis and 415 K for the higher energy photolysis, and the dashed lines are the unbiased prior distributions, which have no adjustable parameters other than the scale factor. We have weighted the prior distributions according to the population of HNCO rotational states present in our thermal gas sample, assuming that HNCO is a prolate symmetric top and that we excite exclusively the $K = 0 \rightarrow 1$ transition and all possible J states within the $K = 0$ sublevel. The prior distribution is clearly too energetic to describe our data, but

TABLE 1: NCO ($X^2\Pi$) Vibronic-State Populations in the Photolysis of HNCO

vibronic state	energy, ^a cm ⁻¹	populations ^b for excess photolysis energy, cm ⁻¹				
		890	1135	1950	2250	3030
(000)						
$^2\Pi_{3/2}$	0	1	1	1	1	1
$^2\Pi_{1/2}$	94.8	0.46	0.62	0.96	0.94	0.82
(010)						
$\mu^2\Sigma^+$	488.7	0.04	0.03	0.16	0.26	0.25
$^2\Delta_{5/2}$	534.5	0.24	0.24	0.81	0.81	1.04
$^2\Delta_{3/2}$	628.3	0.11	0.14	0.68	0.46	0.75
$\kappa^2\Sigma^-$	669.6	0.03	0.02	0.13	0.16	0.17
(020)						
$\mu^2\Pi$	989.5	0.02	0.03	0.25	0.26	0.60
$^2\Phi_{7/2}$	1051.0	0.03	0.08	0.52	0.58	0.89
$^2\Phi_{5/2}$	1143.6	0.08	0.11	0.48	0.59	0.76
$\kappa^2\Pi$	1220.2	<0.01	<0.01	0.25	0.20	0.68
(030)						
$\mu^2\Sigma^-$	1466.7			0.01	0.08	0.29
$\mu^2\Delta$	1495.3			0.04	0.09	0.27
$^2\Gamma_{9/2}$	1571.7			0.10	0.16	0.59
$^2\Gamma_{7/2}$	1661.4			0.10	0.13	0.44
$\kappa^2\Delta$	1763.5			0.02	0.08	0.32
$\kappa^2\Sigma^+$	1777.9			0.08	0.20	0.13
(040)						
$^2H_{11/2}$	2091.6				0.05	0.35
$^2H_{9/2}$	2179.0				0.04	0.22
(050)						
$^2I_{3/2}$	2609.2					0.09
$^2I_{11/2}$	2693.2					0.07
(100)						
$^2\Pi_{3/2}$	1273.0			0.06	0.08	0.28
$^2\Pi_{1/2}$	1362.4			0.05	0.05	0.12
(110)						
$^2\Delta_{5/2}$	1828.2			<0.01	0.01	0.11
$^2\Delta_{3/2}$	1909.0			<0.01	0.03	0.14
(120)						
$^2\Phi_{7/2}$	2364.4					0.05
$^2\Phi_{5/2}$	2437.5					0.03
(001)						
$^2\Pi_{3/2}$	1920.6					0.05 ^c
$^2\Pi_{1/2}$	2017.7					0.02 ^c
(011)						
$^2\Delta_{5/2}$	2440.0					0.02 ^c
$^2\Delta_{3/2}$	2534.8					0.005 ^c

^a Reference 18. ^b Uncertainty is $\pm 20\%$. ^c Estimate based on an assumed value for the Franck–Condon factor.

the more flexible Boltzmann distribution does quite well. Even if we allow the maximum available energy to vary as a fit parameter, the prior distribution does not fit the data as well as the Boltzmann distribution. We used the Boltzmann distribution in all of our analysis, and we report rotational populations for all NCO bands in terms of temperature.

Determining reliable rotational temperatures for the higher lying vibrational bands is more difficult. The spectral congestion, even at very modest photolysis energies, makes extracting rotational distributions difficult even for the (010) states. Rather than trying to fit the data for these bands to specific rotational temperatures, we estimated the dependence of the best fit rotational temperature on the available energy. The only band which has little enough congestion from overlap with other bands for us to observe intensities of individual lines is the (000) $^2\Pi_{1/2}$ band at the red end of the $A(0v_20) \leftarrow X(0v_20)$ spectrum, where we can measure rotational populations even at higher photolysis energies. We measured the rotational temperatures in this state and fit them to a linear dependence on the available energy. These rotational temperatures appear at the bottom of

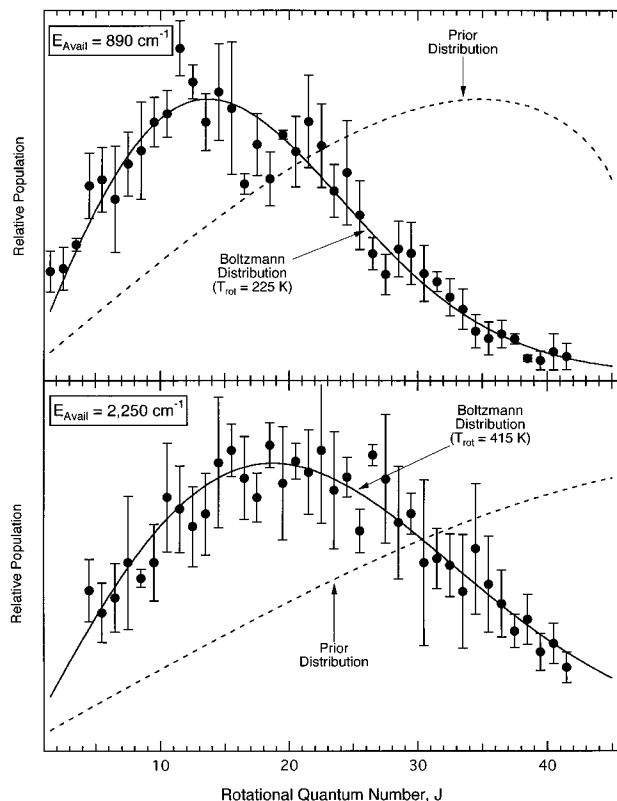


Figure 4. Average intensities of rotational lines from three different branches in the (000) ${}^2\Pi_{1/2}$ state of NCO produced at $E_{\text{avail}} = 890$ and 2250 cm^{-1} . The solid lines are fits to Boltzmann distributions with a temperature of 225 K for the 890- cm^{-1} data and 415 K for the 2250- cm^{-1} data. The dashed lines are the predictions of a purely statistical prior distribution.

Table 2. We extrapolated the rotational temperature for the higher lying vibrational states at each photolysis energy from the rotational temperature determined for the (000) ${}^2\Pi_{1/2}$ state, the available energy for each vibrational state, and the dependence of the rotational temperature on available energy. The resulting simulations appear visually correct, and changing the predicted rotational temperature by ± 50 – 100 K makes the simulated spectra noticeably worse.

The rapid increase in the vibrational excitation of the NCO fragment with increasing photolysis energy is evident in Figure 5, which displays the $A(0\nu_2 0) \leftarrow X(0\nu_2 0)$ region of the NCO LIF spectrum for excitation of three different D vibrational bands in the photolysis of HNCO at 860, 1950, and 3030 cm^{-1} above the dissociation threshold. The strongest excitation in all of the distributions is the bending mode, with excitation evident up to $\nu_2 = 5$. For the $\nu_2 = 4$ and $\nu_2 = 5$ states, the bands are quite weak, and the congestion from numerous bands, both

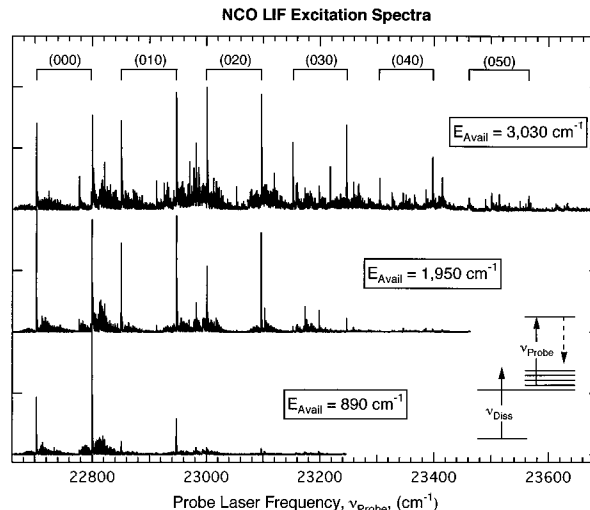


Figure 5. Experimental LIF spectra of NCO fragments produced from photolysis of HNCO in three separate D bands at $E_{\text{avail}} = 890$, 1950, and 3030 cm^{-1} . The increase in excitation of the bending mode with increasing photolysis energy is apparent.

diagonal and off-diagonal, makes assignments very difficult. For photolysis energies that populate these two vibrational states, we simulated only the most intense structure of the $K = \nu_2 + 1$ states. The resulting vibrational state populations are in Table 1.

The photolysis does not populate the stretching modes, ν_1 and ν_3 , of the NCO fragment as efficiently as the bend. Figure 6 is the LIF spectrum of the NCO fragment from the photolysis at 3030 cm^{-1} , displaying the $A(0\nu_2 0) \leftarrow X(1\nu_2 0)$ and $A(0\nu_2 0) \leftarrow X(0\nu_2 1)$ bands as well as the $A(0\nu_2 0) \leftarrow X(0\nu_2 0)$ bands. The Franck–Condon factors for the transitions from $\nu_1'' = 1$ to $\nu_1' = 0$ and $\nu_3'' = 1$ to $\nu_3' = 0$ on the left-hand side of the spectrum are not as strong as the diagonal transitions between $\nu_1'' = 0$ and $\nu_1' = 0$ and $\nu_3'' = 0$ and $\nu_3' = 0$ on the right-hand side. We have taken into account the decrease in our partially saturated line strengths⁴² for the $A(0\nu_2 0) \leftarrow X(1\nu_2 0)$ structure based on the calculated Franck–Condon factor for this transition from Sauder *et al.*³² The magnitude of the vibrational overlap integral from $\nu_1'' = 1$ to $\nu_1' = 0$ is 0.435, compared to a value of 0.890 for the diagonal transition.³² The $A(0\nu_2 0) \leftarrow X(1\nu_2 0)$ structure in the middle of Figure 6 includes this difference such that its intensity reflects the population in $X(1\nu_2 0)$ when compared to the diagonal $A(0\nu_2 0) \leftarrow X(0\nu_2 0)$ bands. The Franck–Condon factors for $A(0\nu_2 0) \leftarrow X(0\nu_2 1)$ are not available.³² Unless these factors are anomalously small, the low intensity of the $A(0\nu_2 0) \leftarrow X(0\nu_2 1)$ transition on the left side of Figure 6 reflects a significantly smaller population in the $\nu_3'' = 1$ states than in excited bending states at comparable energies. For the sake of comparison, we use the same scale factor for the $\nu_3'' = 1$ bands

TABLE 2: Energy Partitioning in NCO($X^2\Pi$) vs Excess Photolysis Energy^a

	energy partitioning						
	excess photolysis energy, E_{avail} , cm^{-1}						impulsive limit ^c
	890	1135	1950	2250	3030	14 100 ^b	
$\langle f_{\text{bend}} \rangle^f$	0.24	0.21	0.30	0.28	0.31	0.26 ^e	0.310
$\langle f_{\text{stretch}} \rangle$	0	0	0.01	0.01	0.02		0.105
$\langle f_{\text{rot}} \rangle$	0.10	0.07	0.04	0.05	0.04	0.04	0.400
$\langle f_{\text{trans}} \rangle$	0.66	0.72	0.65	0.66	0.63	0.70	0.185
$T_{\text{rot}} ({}^2\Pi_{3/2})$, ^d K	225	225	325	415	480		

^a Typical uncertainty in the fractions is $\pm 20\%$. ^b Reference 26. Measured by H atom center-of-mass kinetic energy at 193.3-nm photolysis. ^c Reference 49. ^d Best fit rotational temperature in the NCO (000) ${}^2\Pi_{3/2}$ state. ^e Sum of vibrational excitation in both stretching and bending modes. ^f $\langle f_i \rangle = \langle E_i \rangle / E_{\text{avail}}$.

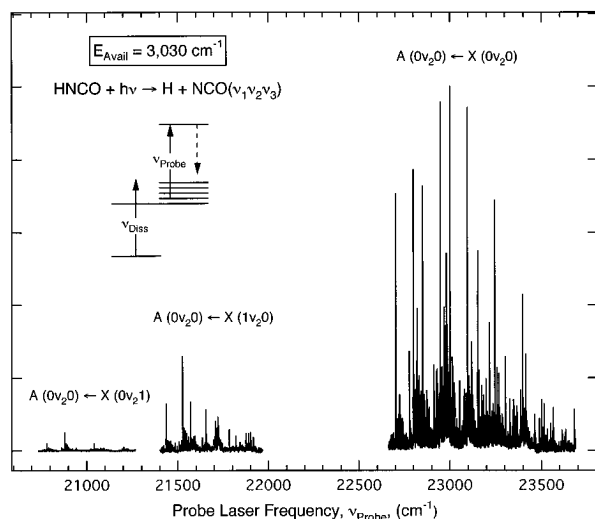


Figure 6. Comparison of the LIF spectra of NCO fragments probing the $(0v_2,0)$, $(1v_2,0)$, and $(0v_2,1)$ bands. The $A(0v_2,0) \leftarrow X(1v_2,0)$, $(0v_2,1)$ bands are scaled to account for the difference in the Franck–Condon factors between the $A(0v_2,0) \leftarrow X(1v_2,0)$ and $A(0v_2,0) \leftarrow X(0v_2,0)$ bands. The Franck–Condon factor for the $A(0v_2,0) \leftarrow X(0v_2,1)$ bands is unknown, and we took them to be the same as those for the $A(0v_2,0) \leftarrow X(1v_2,0)$ bands for the sake of comparison.

as for the $v_1'' = 1$ bands in Figure 6, but because the actual Franck–Condon factors for these bands are unknown, our analysis does not accurately determine the populations for the $(0v_2,1)$ states. As with the higher lying $(0v_2,0)$ bands, we have simulated only the structure belonging to the $K = v_2 + 1$ vibronic states for excitation of v_1 and v_3 , and we present the vibrational-state populations in Table 1.

IV. Discussion

The internal energy distribution of the NCO fragment contains information about the photodissociation dynamics and about the nature of the excited electronic state in the parent HNCO molecule. The simplest quantity characterizing the dissociation is the amount of available energy after the photolysis, which in turn depends on the actual value of the threshold for dissociation of the N–H bond, a quantity having an uncertainty of several hundred wavenumbers (Figure 1).⁷ The appearance threshold for NCO fragments in our experiment is consistent with the reported value of the dissociation energy, but we cannot reduce the uncertainty in this quantity. Our room-temperature sample has significant rotational excitation, amounting to approximately 100 cm^{-1} on average, which is comparable to the measured uncertainty in the value of the bond dissociation energy. There is also a strong likelihood that there is a photolysis signal from vibrational hot band transitions in our photolysis yield spectra. The lowest vibrationally excited state in HNCO is the 577-cm^{-1} *cis* bend,⁴⁸ which has a population of about 6% compared to the ground state in our 300 K sample. Because of the geometry change upon excitation, hot band transitions from an excited bending state are likely to have favorable Franck–Condon factors and contribute significantly to the photolysis signal. In fact, we find population in states of the NCO fragment that lie above the total excess photolysis energy as measured by the difference between the photon energy and the literature value of the dissociation energy, suggesting the participation of hot bands.

The rather diffuse spectra in Figure 1 display both vibrational and coarse rotational structure. Our photolysis laser line width, which is on the order of 0.1 cm^{-1} , does not limit the width of the features in the spectrum. The observed width seems to

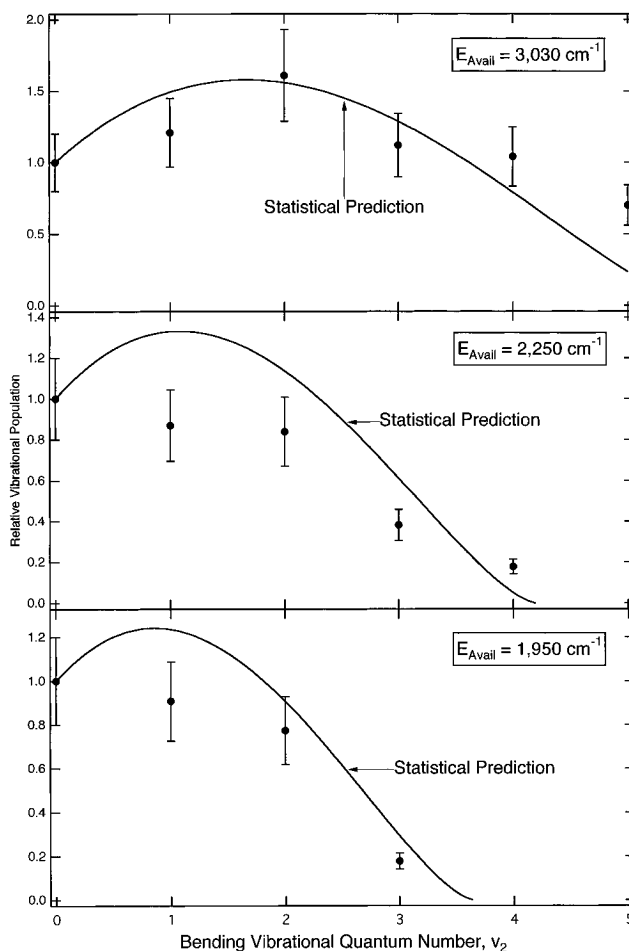


Figure 7. Vibrational-state populations in the NCO bending mode summed over all of the states in a given v_2 manifold for three different photolysis energies. The solid lines are the predictions of an unbiased prior distribution.

reflect the lifetime of the excited state, and, consistent with such lifetime broadening, increases with photolysis energy. Because the extensive congestion in the spectrum prevents the measurement of the line width of an isolated rotational transition, we can establish only an upper limit to the lifetime of the excited state of HNCO. In separate double-resonance measurements of widths of single rotational lines in the NCO photolysis yield spectrum,⁴¹ we obtain a width of about 1.8 cm^{-1} in the energy region of the inset of Figure 1, corresponding to an excited-state lifetime of 3 ps.

The change in the geometry of the NCO group from linear in the ground state to bent in the excited state produces a significant force along the bending coordinate during the dissociation. The comparison between the populations of excited stretching states in NCO compared to isoenergetic excited bending states illustrates this point. For example, Table 1 shows that in the dissociation at $E_{\text{avail}} = 3030 \text{ cm}^{-1}$, the population of the $(020) \Phi$ states is more than 4 times the population of the corresponding Π states in the (100) manifold. Likewise, the ratio of the populations in $(030) \Gamma$ and $(110) \Delta$ is also approximately 4, and the ratio of $(040) \text{H}$ to $(120) \Phi$ is more than 7. A purely statistical dissociation would populate each of these sets of states nearly equally since they have the same degeneracy and roughly the same energy.

Figure 7 is a plot of the distribution of population in the bending states as a function of v_2 for the three highest photolysis energies. The populations are sums over all of the states in a single v_2 manifold relative to the population in $v_2 = 0$. For $v_2 = 4$ and 5, where we have only measured the population in the

$K = v_2 + 1$ states, we estimate the population summed over all of the states in the manifold from the amount of signal in the states that we measured and the amount of the total population represented by these states in $v_2 = 0, 1, 2,$ and 3 . The error bars on the points are $\pm 20\%$ of the measured values, based on the uncertainty measurement described above. The smooth lines in these plots are the predictions of the unbiased prior distribution, considering excitation only in the bending mode. We approximate this distribution as a function of the vibrational energy by treating both the vibrational and rotational energies as continuous variables and integrating over the rotational distributions. The result is that the vibrational-state population depends on the difference between the available energy and the vibrational energy,⁴⁶

$$P^0(v_2) \propto 2(v_2 + 1)(E_{\text{avail}} - E_{\text{vib}})^{3/2}$$

The $2(v_2 + 1)$ factor is the degeneracy of the vibrational state. The distributions are quite close to the statistical prediction, especially for the highest energy photolysis with $E_{\text{avail}} = 3030 \text{ cm}^{-1}$. For the other two energies, the actual distributions are slightly less energetic than the prior distribution. The statistical calculations do a much poorer job of predicting the amount of vibrational excitation in the symmetric stretch, overestimating the population in this mode by a factor of 2–4. It is clear that the vibrational excitation results from the forces present on the dissociative potential energy surface, which should be much stronger in the bending coordinate than in the symmetric or antisymmetric NCO stretches. The rotational state distributions in Figure 4 are also less energetic than a purely statistical model predicts. Both the vibrational and rotational distributions suggest that the force of the dissociation, rather than a statistical partitioning of energy, determines the internal energy content of the NCO fragment.

Table 2 summarizes the energy partitioning at the five different photolysis energies as a function of the total energy. For comparison, Table 2 also contains the energy partitioning data from the work of Zhang *et al.*,²⁶ who photolyzed HNCO at 193.3 nm in a molecular beam and measured the kinetic energy distribution of the H atom fragment. Our results at lower photolysis energies are generally consistent with theirs. We find approximately 35% of the energy in internal degrees of freedom at $E_{\text{avail}} = 1950, 2250,$ and 3030 cm^{-1} , with approximately 30% in vibration and 5% in rotation. There is proportionally less energy in vibration and more in rotation closer to threshold. The major of the vibrational energy appears in the bend, and less than 2% appears in excited stretching states. The results of the 193.3-nm photolysis show a slightly larger fraction of the total energy, 70%, in translation.

Table 2 also presents a classical calculation⁴⁹ of the energy partitioning in the impulsive limit. Because this model does not account for the forces along the NCO bending coordinate during the dissociation, it predicts little vibrational excitation. Indeed, we find very little energy in the stretching vibrations but substantial amounts in the bending vibration. The calculated fraction of rotational excitation in NCO is small (2% of the available energy) as a result of the small torque that the light H atom exerts on the NCO fragment. The experimental rotational excitation is also small for large excess photolysis energies but never decreases to the impulsive limit even at very high energies, where the limiting experimental value is 4%. Our results, which are for a lower available energy than those of Zhang *et al.*,²⁶ have a slightly smaller fraction of energy in translation and larger fraction in rotation, consistent with the dissociation being somewhat less strongly impulsive from the region of the dissociative potential that our excitation reaches.

For comparison, the energy partitioning in the statistical limit for $E_{\text{avail}} = 3030 \text{ cm}^{-1}$ also appears in Table 2. Unlike the impulsive model, the partitioning in the prior distribution depends on the amount of available energy, with the fraction in NCO internal energy increasing steadily with available energy. As we noted above, the statistical calculation predicts the excitation in the NCO bend quite well but fails to accurately predict the amount of energy in other vibrations, NCO rotations, or relative translation. Clearly, an accurate description of the dissociation requires a more complicated dynamical model that includes the forces in the exit channel. Except for the bend, the experiment finds more energy in NCO internal degrees of freedom than the impulsive model predicts and less than the prediction of the prior distribution. The impulsive model describes state distributions well if the excited-state potential energy surface is purely repulsive, and the prior distribution does well for a long-lived excited electronic state with no interaction as the products separate. Our results show that HNCO is predissociative at energies near the N–H dissociation threshold, indicating the presence of a well on the excited-state surface. The partitioning of large amounts of energy into the NCO bending mode and the relative translation of H and NCO fragments suggests that there are strong forces along both the N–H and the NCO bending coordinates on the dissociative surface.

V. Summary

We report the direct observation of the internal energy distribution of the NCO fragment from photolysis of HNCO at five different energies near the threshold for cleavage of the N–H bond. We probe the NCO fragment by LIF on its $A \leftarrow X$ transition.^{18,36,37} The photolysis yield spectrum, in which we fix the probe laser wavelength on a transition in the NCO fragment and scan the photolysis laser through the UV absorption bands of the parent HNCO, shows clear rotational and vibrational structure, particularly at lower photolysis energies. In separate double-resonance experiments,⁴¹ we have measured the lower limit to this lifetime to be 3 ps at $38\,500 \text{ cm}^{-1}$. Here, we excite five different vibrational bands up to 3030 cm^{-1} excess photolysis energy. A Boltzmann distribution fits the rotational-state populations well, and the overall rotational excitation is much less than predicted by a simple statistical model. Vibrational energy appears primarily in the bending mode of the NCO fragment, with the population in excited bending states exceeding that in nearly isoenergetic excited stretching states by a factor of 6 or more. The small population in the symmetric stretch shows that the dissociation is very nonstatistical, and the preference for partitioning of energy into the NCO bending mode is a result of the dissociation from a bent NCO group in the A'' state of HNCO to a linear NCO fragment where the force in the NCO bending coordinate strongly excites the bend. Overall, about 65% of the total energy appears in relative translation of the fragments at all of these near-threshold photolysis energies, while approximately 30% goes into vibration (dominated by the bending excitation) and 5% into rotation.

Acknowledgment. We thank the Division of Chemical Sciences of the Office of Basic Energy Sciences of the Department of Energy for supporting this work. In addition, we thank Professor Paul Dagdigian for graciously supplying us with his programs to simulate the LIF spectrum of the NCO fragment. These programs, along with the prescription for extracting vibrational populations from the spectral simulations, were essential in our analysis.

References and Notes

- (1) Perry, R. A.; Siebers, D. L. *Nature* **1986**, 324, 657.
- (2) Miller, J. A.; Bowman, C. T. *Int. J. Chem. Kinet.* **1991**, 23, 289.
- (3) Mui, J. Y. P.; Back, R. A. *Can. J. Chem.* **1963**, 41, 826.
- (4) Wooley, W. D.; Back, R. A. *Can. J. Chem.* **1967**, 46, 295.
- (5) Bradley, J. N.; Gilbert, J. R.; Svejda, P. *Trans. Faraday Soc.* **1968**, 64, 911.
- (6) Okabe, H. *J. Chem. Phys.* **1970**, 53, 3507.
- (7) Russic, B.; Berkowitz, J. *J. Chem. Phys.* **1994**, 100, 4498.
- (8) Spiglanin, T. A.; Perry, R. A.; Chandler, D. W. *J. Phys. Chem.* **1986**, 90, 6184.
- (9) Brown, S. S.; Berghout, H. L.; Crim, F. F. *J. Chem. Phys.* **1995**, 102, 8440.
- (10) Brown, S. S.; Metz, R. B.; Berghout, H. L.; Crim, F. F. *J. Chem. Phys.*, to be submitted.
- (11) Likar, M. D.; Baggot, J. E.; Sinha, A.; Ticich, T. M.; Vander Wal, R. L.; Crim, F. F. *J. Chem. Soc., Faraday Trans. 2* **1988**, 84, 1483.
- (12) Crim, F. F. *Annu. Rev. Phys. Chem.* **1993**, 44, 397.
- (13) Ram, R. S.; Bernath, P. F. *J. Opt. Soc. Am. B* **1986**, 3, 1170.
- (14) Ubachs, W.; Meyer, G.; Ter Meullen, J. J.; Dymanus, A. *J. Mol. Spectrosc.* **1986**, 115, 88.
- (15) Hack, W.; Mill, T. *J. Mol. Spectrosc.* **1990**, 144, 358.
- (16) Charlton, T. R.; Okamura, T.; Thrush, B. A. *Chem. Phys. Lett.* **1982**, 89, 98.
- (17) Copeland, R. A.; Crosley, D. R. *Can. J. Phys.* **1984**, 62, 1488.
- (18) Patel-Misra, D.; Sauder, D. G.; Dagdigian, P. J. *J. Chem. Phys.* **1990**, 93, 5448.
- (19) Drozdowski, W. S.; Baronovski, A. P.; McDonald, J. R. *Chem. Phys. Lett.* **1979**, 64, 421.
- (20) Fujimoto, G. T.; Umstead, M. E.; Lin, M. C. *Chem. Phys.* **1982**, 65, 197.
- (21) Spiglanin, T. A.; Perry, R. A.; Chandler, D. W. *J. Chem. Phys.* **1987**, 87, 1568.
- (22) Spiglanin, T. A.; Chandler, D. W. *J. Chem. Phys.* **1987**, 87, 1577.
- (23) Spiglanin, T. A.; Chandler, D. W. *Chem. Phys. Lett.* **1987**, 141, 428.
- (24) Bohn, B.; Stuhl, F. *J. Phys. Chem.* **1993**, 97, 4891.
- (25) Yi, W.; Bersohn, R. *Chem. Phys. Lett.* **1993**, 206.
- (26) Zhang, J.; Dulligan, M.; Wittig, C. *J. Chem. Phys.* **1995**.
- (27) Dixon, R. N.; Kirby, G. H. *Trans. Faraday Soc.* **1968**, 64, 2002.
- (28) Rabalais, J. W.; McDonald, J. R.; McGlynn, S. P. *J. Chem. Phys.* **1969**, 51, 5103.
- (29) Rabalais, J. W.; McDonald, J. M.; Scherr, V.; McGlynn, S. P. *Chem. Rev.* **1971**, 71, 73.
- (30) Yamada, K. *J. Mol. Spectrosc.* **1980**, 79, 323.
- (31) Du, K. Y.; Setser, D. W. **1988**.
- (32) Sauder, D. G.; Patel-Misra, D.; Dagdigian, P. J. *J. Chem. Phys.* **1991**, 95, 1696.
- (33) Herzberg, G.; Teller, E. *Z. Phys. Chem. B* **1993**, 21, 410.
- (34) Renner, R. *Z. Phys.* **1934**, 92, 172.
- (35) Hougen, J. T. *J. Chem. Phys.* **1961**, 36, 519.
- (36) Dixon, R. N. *Phil. Trans. R. Soc. London, Ser. A* **1960**, 252, 165.
- (37) Bolman, P. S. H.; Brown, J. M.; Carrington, A.; Kopp, I.; Ramsay, D. A. *Proc. R. Soc. London, Ser. A* **1975**, 343, 17.
- (38) Woodward, D. R.; Fletcher, D. A.; Brown, J. M. *Mol. Phys.* **1987**, 62, 517.
- (39) Wu, M.; Northrup, F. J.; Sears, T. J. *J. Chem. Phys.* **1992**, 97, 4583.
- (40) Hemmerling, B.; Vervloet, M. *Mol. Phys.* **1993**, 78, 1423.
- (41) Brown, S. S.; Berghout, H. L.; Crim, F. F. *J. Chem. Phys.*, in preparation.
- (42) Silver, J. A.; Dimpfl, W. L.; Brophy, J. H.; Kinsey, J. L. *J. Chem. Phys.* **1976**, 65, 1811.
- (43) Linhard, M. *Z. Anorg. Allg. Chem.* **1938**, 236, 200.
- (44) Ashby, R. A.; Werner, R. L. *J. Mol. Spectrosc.* **1965**, 18, 184.
- (45) East, A. L. L.; Johnson, C. S.; Allen, W. D. *J. Chem. Phys.* **1993**, 98, 1299.
- (46) Levine, R. D.; Bernstein, R. B. *Acc. Chem. Res.* **1974**, 7, 393.
- (47) Levine, R. D.; Bernstein, R. B. *Molecular Reaction Dynamics and Chemical Reactivity*; Oxford University: New York, 1987.
- (48) Steiner, D. A.; Wishah, K. A.; Polo, S. R.; McCubbin, T. K. *J. Mol. Spectrosc.* **1979**, 76, 341.
- (49) Tuck, A. F. *J. Chem. Soc., Faraday Trans. 2* **1977**, 73, 689.

JP952667R